Spectroscopic study of laser-produced plasmas in hydrogen

John F. Kielkopf
Department of Physics, University of Louisville, Louisville, Kentucky 40292
(Received 19 January 1995; revised manuscript received 13 April 1995)

A 300-mJ, 7-ns, 1064-nm pulse from a Q-switched neodymium-doped yttrium aluminum garnet laser was tightly focused into H_2 at pressures of the order of 1 atm. or less. Charge-coupled-device images, time-resolved schlieren, and time-resolved spectra from the vacuum ultraviolet through the visible distinguish the prompt centrally localized emission during the initial breakdown from the subsequent blast wave and shock dissociation of the gas. Schlieren images show that the shock wave expands from the center with a velocity in excess of 13 km/s, and then slows to close to sound wave speed within 1.5 μs. Inside the shock front, starting with an initial electron density greater than 4×10^{18} cm^{-3} and a temperature of 10^5 K, the emitting atomic gas cools and leaves a low-density core surrounded by a cylindrical shell of slowly expanding excited H about 1.5 mm from the focal axis after 8 μs. The regions responsible for visible and vacuum ultraviolet emission are in local thermodynamic equilibrium. The density, temperature, and flow agree quantitatively with the predictions of Saha ionization and excitation equilibrium in a cylindrical blast wave with counterpressure. These models characterize the postplasma gas close to the region of breakdown and permit the source to be used for quantitative spectroscopic studies of atomic and molecular processes.

PACS number(s): 52.25.Rv, 52.25.Qt, 52.50.Jm, 52.35.Tc

I. INTRODUCTION

In the years following the development of Q-switched lasers, the breakdown produced by focusing their light into gases was studied intensively. Measurements of the visible spectra, and time-resolved observations of the luminous gas, revealed a highly ionized plasma which expanded somewhat like a blast wave into the surrounding medium. Those first studies dealt with breakdown in air and the rare gases, and the results are summarized by Hughes [1]. More recently, the application of this phenomenon to short wavelength lasers, laser ablation, and spectrochemical analysis has stimulated basic research with other gases, solid targets, and higher laser energies [2,3].

Our interest is in using the transient plasma and the postbreakdown partially ionized or dissociated gas as a subject for studies of atom-atom and atom-molecule collisions. For example, luminous shock tube [4,5] and T-tube [6] experiments have been used to measure dissociation, broadening by neutral atomic H collisions, and ion-electron Stark broadening. In principle, laser produced plasmas offer the advantages of low impurity concentrations, high repetition rate, stability, the absence of electrical noise, and scalability to high densities where collision rates are high. This will help to produce local thermodynamic equilibrium quickly. In order to utilize the source in this way, we need a reliable model of its time-dependent radial structure. In spite of the work that has been reported recently, the development of the plasma for laser energies and gas pressures close to threshold appears to be incompletely understood. Particularly for gaseous H_2 targets, there is a notable lack of information on the plasma conditions just after breakdown, the spatial distribution and its change with time, or the condition of the gas long after the plasma has cooled below a temperature at which excited atomic states are populated. The experiments which are reported here describe the appearance of the plasma during its radiative phase and draw comparisons to blast wave theories of shock propagation. Self-focusing during the initial excitation pulse and the unusual hydrodynamics of the postplasma gas will be discussed elsewhere.

II. EXPERIMENTS

A. Instrumentation

A Continuum Surelite II-10 Q-switched neodymium-doped yttrium aluminum garnet (Nd:YAG) laser produces 6-ns pulses at 1064-nm. Its far field 300-mJ Gaussian beam with a burn pattern diameter of 6 mm is directed through an 8 cm focal length suprasil fused silica lens and into a 40 mm inside diameter, five-way, stainless steel high-vacuum cross. The cross is closed with four optical quality suprasil windows on orthogonal axes, and a fifth optical quality sapphire window directly above the plasma region. Figure 1 shows the arrangement looking down on the plasma through the sapphire window. It is evacuated by a liquid nitrogen trapped high-vacuum system which includes a residual gas analyzer for leak and impurity detection. H_2 with 99.999% purity from Spectra Gases is introduced into this chamber through stainless steel tubing, a 2-μm porous stainless steel particle filter, and an optional secondary cold trap.

The transmission of the Nd:YAG pulse through the chamber is measured by placing a Scientech Model 380101 volume absorbing calorimeter at the output window of the cell. Cell pressures are monitored with ca-

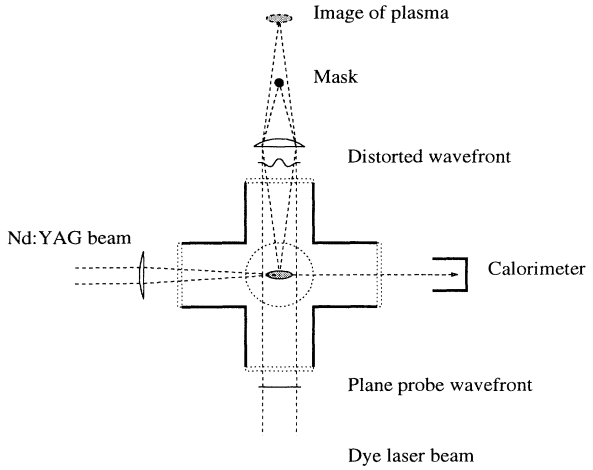

FIG. 1. A view of the experiment from the top. The Nd:YAG plasma-production beam enters from the left and is focused at the center of the cross. A spatially filtered, expanded, and collimated dye laser beam passes through the discharge region and produces a schlieren image of the shock. Visible and ultraviolet spectra are recorded through an optical system looking downward.

pacitive manometers. The cell is cleaned in an ultrasonic bath, rinsed with distilled water and methanol, and then dried to remove dust and surface contamination. After the cell is pumped, purged, and filled with H_2 it is sealed off from the vacuum and gas handling systems, except for a connection to the manometer. For a fill pressure of 700 Torr there is a slight (2–4 Torr) increase in pressure after the laser has been running for several hours which is due to heating of the gas by absorption of the laser energy. The pressure returns at equilibrium to the filling pressure after the laser is turned off. With these precautions, the optical spectrum from Lyman-α through Balmer-α is free of impurity emission lines.

Schlieren images of the plasma and postplasma heated gas were produced by illuminating the cell at right angles to the excitation laser with a pulsed dye laser as shown in Fig. 1. Light from a second Quantel/Continuum YG661 Nd:YAG laser was frequency doubled and used to excite a dye laser (0.007 Å full width at half maximum) and longitudinal amplifiers. For these experiments, the dye laser was running with sulforhodamine 640, and was tuned to wavelengths $\approx$ 6100 Å where absorption by the plasma is low. Its 2-mJ pulse was spatially filtered, collimated, and directed through the plasma. The light was then refocused onto a small ball bearing or a sharp straight edge to block the unperturbed beam and pass only light deviated by the plasma in the usual schlieren configuration [7]. Schlieren images were recorded with a Kodak KAF-0400 768 × 514 full frame charge-coupled device (CCD) cooled by a Peltier refrigerator to reduce thermal dark noise to a level of $15e^-$ per pixel [8]. Time resolution in the schlieren measurements was achieved by synchronizing the two Nd:YAG lasers with a Stanford Research Systems DG535 four-channel pulse generator. The delay between the plasma forming Nd:YAG pulse and the dye laser excitation pulse could be controlled with a limiting accuracy of about 10 ns due to triggering uncertainty in the YG661 electronics. The same camera system, with imaging optics instead of the schlieren illumination, also recorded the time-averaged emission from the plasma directly.

The vacuum ultraviolet emission from the plasma was studied through MgF_2 windows with an Acton VM502, 0.2 m focal length monochromator equipped with a 1200 groove/mm holographic iridium-coated concave grating, slit widths and masks set to provide 4-Å resolution, and an EMI G-type solar-blind CsI photomultiplier. The ultraviolet and visible emission spectra were recorded with a 0.25 m Czerny-Turner, toroidal mirror, 1200 groove/mm plane grating, imaging spectrometer with 3-Å spectral resolution. The spectral response of this instrument with an EMI 9789Q photomultiplier rises slowly from 2000 Å, peaks at 5000-Å, and decreases rapidly for wavelengths greater than H_α. At long wavelengths Schott glass filters eliminated second order contamination. The vacuum ultraviolet spectra were spatially integrated over the emitting volume of the plasma, but the ultraviolet-visible spectra yielded spatial as well as spectral resolution by a sapphire lens optical system which imaged the plasma with a 10× magnification onto a slit mask parallel to the plasma axis as shown in Fig. 2. A field lens (not shown in the figure) behind the mask reimaged the transfer optics onto the entrance slit of the monochromator to optimize the flux passing through the system. The photomultiplier outputs were preamplified with a Stanford Research Systems SR240 300-MHz fast preamplifier, and then sampled with a Stanford gated integrator. Simultaneously, the outputs were digitized and displayed on a Tektronix 2230 100-MHz oscilloscope. An 80486 computer system running 32-bit FORTH in protected mode provided instrument control and data acquisition for the experiment.

B. Images and photometry

Figure 3 shows a magnified view of the emission from the plasma integrated over the duration of a single shot. The cell was filled at room temperature with H_2 at

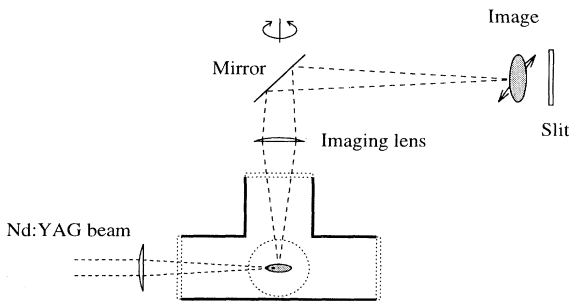

FIG. 2. A view of the experiment from the side. The rotation of the mirror about a vertical axis selects an offset for recording spectra at different distances from the plasma axis.

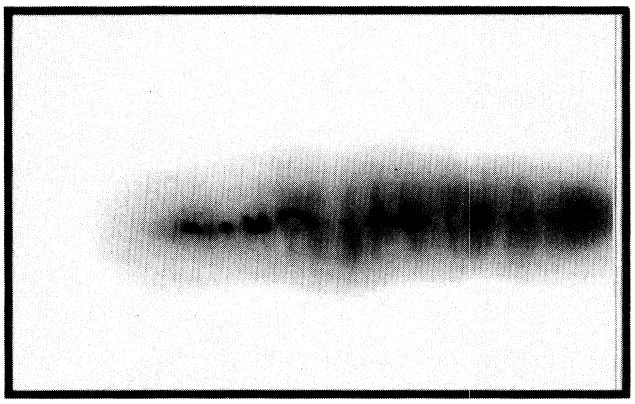

FIG. 3. A plasma in 2.2×10^{19} cm^{-3} H_2 produced by a 300-mJ 1064-nm Nd:YAG focused laser pulse entering from the right. The border defines a region 6×4 mm^2.

606 Torr, an initial molecular density of 2.2×10^{19} cm^{-3}. The laser was focused on a point at the center of the image, but at this pressure and these laser energies self-focusing moves the breakdown point toward the lens. In this negative image, the black spots are regions of intense emission. They are characteristic of breakdown at pressures this high, although they are rarely present at pressures below 300 Torr. The spots are not fully resolved in these images, and must have a true size less than 20 μm across. Most of the light emitted by the plasma over the entire duration of the spark originates from a cylindrical region less than 1 mm in diameter and 5 mm long. Time-resolved measurements described below show that this emission results from a propagating cylindrical shock front that moves radially outward from the axis. On the axis, the bright spots develop at the moment of breakdown and appear to be the origin of this front.

Absolute photometry from these images is possible because the quantum efficiency of the CCD is known, as are the collection solid angle and the transmission of the optical system. However, since the CCD is sensitive only to a portion of the frequency range over which the plasma radiates, the photometric measurement only sets a lower bound on the radiated energy. For the image shown in Fig. 3, the plasma emitted no less than 0.6 mJ between 400 nm and 1 μm. We will see from the spectra that all of this emission is in the Balmer series or a continuum primarily due to recombination of plasma ions and electrons. Consequently, for each photon emitted in the visible there will also be one emitted at Lyman-α which will not be detected by the CCD. With allowance for this, the total radiated energy from the plasma is 4 mJ.

In Fig. 4 the fraction of the incident laser energy that is absorbed by the plasma increases with pressure from less than 100 Torr at the first appearance of breakdown up to 700 Torr where 84% of the incident laser energy is removed from the beam. Thus at the highest pressures $E_0 = 230$ mJ is coupled into the gas. This critical energy determines the scaling in blast wave theories and also sets limits on the degree and extent of dissociation of H_2 and

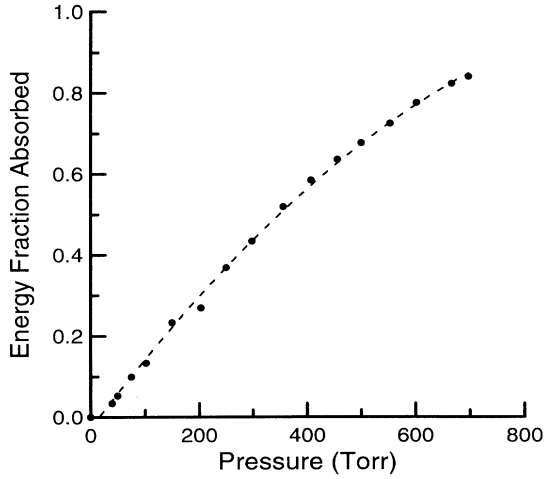

FIG. 4. Fraction of the incident 1064-nm laser energy absorbed for different pressures of H_2. The incident energy was 272 mJ at the focal point.

ionization of the atomic H in the plasma volume. From the 4 mJ accounted for by CCD photometry, less than 2% of the absorbed energy from the Nd:YAG reappears as emitted light from the plasma.

C. Spectra

The ultraviolet-visible spectrum of the axial emission from the plasma is shown in Fig. 5 at several different delays after the arrival of the Nd:YAG excitation pulse. Initially only a broad continuum is apparent through most of the visible, although the H_α line, not shown in this figure, appears distinctly. For the least possible delays H_β is so wide that it disappears as an identifiable

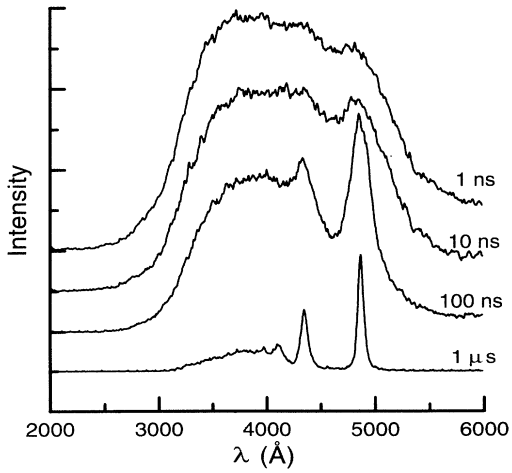

FIG. 5. Spectra of the plasma at breakdown, and 10 ns, 100 ns, and 1 μs later for an initial density of 2.1×10^{19} cm^{-3} H_2, and a 300-mJ 1064-nm pulse. The time resolution gate width was 1 ns.

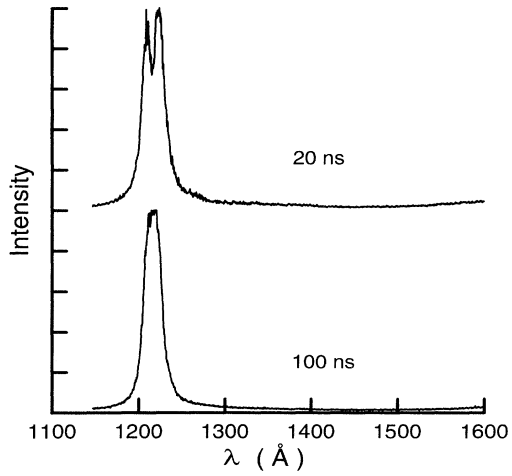

FIG. 6. Vacuum ultraviolet spectra of the plasma 20 ns and 100 ns after breakdown. L_α is strongly reversed when the plasma forms, but the reversal decreases and the line becomes more intense later.

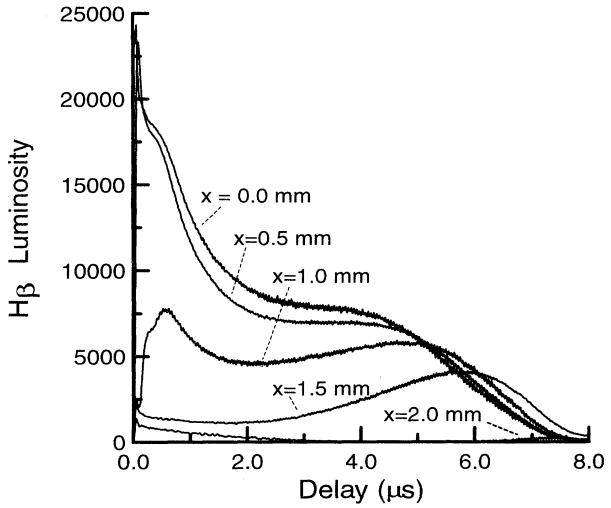

FIG. 7. Time dependence of the emission at the wavelength of H_β (4861 Å), for different offsets from the excitation laser axis.

feature. H_β emerges from the blend of the continuum and other Balmer lines shortly after the Nd:YAG pulse has stopped. Higher lines of the series appear in succession as the plasma electron density decreases and the bremsstrahlung and recombination continua decline. For the most part, the visible spectrum is otherwise featureless. Any structure seen in Fig. 5 other than the Balmer series is noise. A very protracted high signal-to-noise search was conducted for evidence of emission from the H_2 molecule at times from 1 to 10 μs without success. Evidently, whenever and wherever the plasma is hot enough to excite H_2, the molecule is also promptly dissociated into free atoms.

The vacuum ultraviolet spectrum in Fig. 6 only exhibits Lyman-α, associated atomic continua, and an extension of the bremsstrahlung-recombination continuum into the vacuum ultraviolet from the Balmer series limit. In the earliest phases, a few nanoseconds after breakdown, Lyman-α is optically thick, reversed, and not very strong. By 20 ns, the reversal has decreased, and after 100 ns it is not apparent at this spectral resolution although the line shape is still characteristic of self-absorption. The Lyman-α profile and details of the origin of features in the continuum have been described in a preliminary report, and will be treated in detail elsewhere [9].

In the discussion which follows, it is helpful to think of velocity in units of mm/μs, equivalent to μm/ns or, conveniently, km/s. With a monochromator set to monitor the center of H_β, the dependence on time of the plasma luminosity at 4861 Å is shown in Fig. 7 for selected offsets from the axis of the Nd:YAG excitation laser. Summing over a region 0.25 mm across the axis there is fast emission with a rise time of the order of 10 ns. This prompt spike is attributed to the breakdown on the focal axis. In a region centered 0.5 mm off the axis, the intense prompt spike is replaced by a slowly growing emission, delayed from the prompt feature by about 50 ns. A cross section of the image in Fig. 3 shows a hot central core about 0.2 mm in diameter which would lie within the aperture used for the time-dependent measurement in Fig. 7. The delayed pulse off the axis is identified with a luminous shock wave. The spatial resolution of the spectral imaging is not sufficient to derive a very accurate velocity from these observations, but it appears that the luminous region is propagating outward at approximately 7 km/s around 100 ns after the first emission appears during breakdown. The thin shell remains detectable for about 300 ns when it is approximately 1 mm from the axis. The weak fast spike seen in the data for 2 mm offset is an artifact from scattered light. The spectrum of this spike is the same as that of the central emission.

Figure 7 shows other structure as well. Offset 1 mm from the axis and 0.8 μs after breakdown there is a broad intensity maximum that results from the decreasing width of H_β. The spectrometer is recording the intensity at the center of the line, which will increase as the linewidth decreases if the emission rate is constant. In this case, the emission rate is falling but the decreasing linewidth, due to a decline in the electron density, compensates and leaves a flat region or a small peak. After about 5 μs the intensity declines rapidly. At this time the H_β width is of the same order as the instrumental response, and the detected decline is due to a real reduction in the H_β emission. Except near the edges, the reduction occurs simultaneously across the entire plasma volume. The edges remain somewhat brighter than the center after 6 μs, giving a shell-like appearance to the fading plasma.

The apparent distribution is actually the integral along a line of sight through a nominally cylindrically symmetric plasma [10]. The true radial distribution of H_β luminosity can be found by an Abel inversion of these data. The result of this calculation is shown in Figs. 8 and 9.

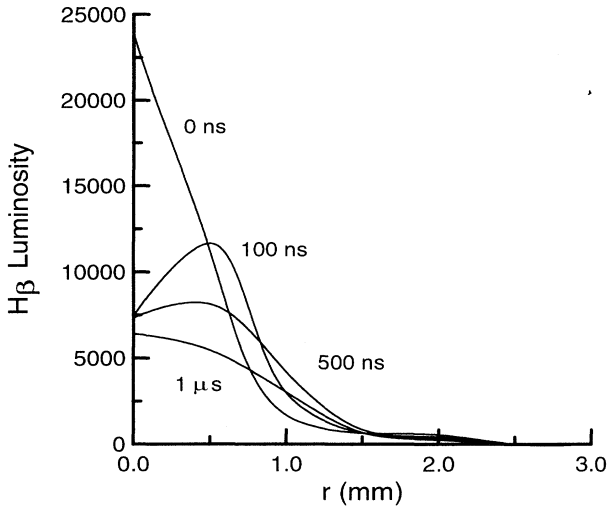

FIG. 8. Radial dependence of H_β luminosity from Abel inversions of the observed luminosity for delays up to 1 μs after breakdown.

As noted by Griem [10] and Hutchinson [11] the inversion is sensitive to noise because it depends on the spatial derivative of the measurement. The original data were recorded with a resolution of 0.25 mm, interpolated to finer spacing by polynomial fitting, Abel inverted, and then sampled on a 0.5-mm spacing in order to minimize the effects of noise. The inverted measurements were spline interpolated for the figure to give a smooth appearance, but they are only valid within the 0.5-mm sampling resolution. As in the line of sight data, the Abel inversion reveals a sharply defined shell which moves rapidly outward to a radius of about 0.6 mm after 100 ns. By 6 μs a dark center is surrounded by a 1.5 mm radius shell. There is evidence of radial flow in the progression of the luminosity peak outward from 4 to 8 μs after breakdown. A typical flow velocity during this time is 0.4 km/s, well below the speed of sound.

D. Schlieren

Radial expansion is very evident in the schlieren measurements shown in Fig. 10, where the observations are more sensitive to regions of high density in the shock front. The time axis reference is set to zero by identifying the delay at which no schlieren can be seen. The uncertainty in this setting is the 10 ns jitter in the relative triggering of the lasers. On the other hand, the luminosity measurements are triggered by the Nd:YAG pulse itself, and have no significant jitter. The reference zero for those measurements is the first moment at which emission from the plasma can be detected in the rising pulse on axis. The ambiguity, a few nanoseconds, is less than the rise time. When both luminosity and schlieren measurements are plotted on the same scale, as in Fig. 10, it is clear that the schlieren measurements are of a region outside the luminous zone. The shock front itself apparently does not immediately radiate, but propagates outward and leaves behind a rarefied gas which radiates soon thereafter.

A numerical derivative of the schlieren curve shows a decelerating shock front. At the earliest moments for a valid measurement, the front velocity is of the order of 13 ± 5 km/s, but with a very large uncertainty because of timing jitter. Later the data are not sensitive to the time zero point, but the velocities are also lower. When the shock wave is 5 mm from the axis 1.5 μs after breakdown its speed is only about 2.0 ± 0.2 km/s, slightly greater than the speed of sound in H_2 which is 1.3 km/s.

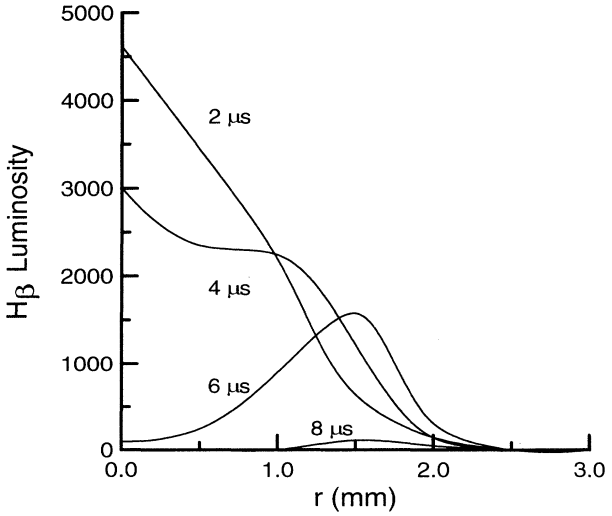

FIG. 9. Radial dependence of H_β luminosity from Abel inversions of the observed luminosity for different delays 2 to 8 μs after breakdown.

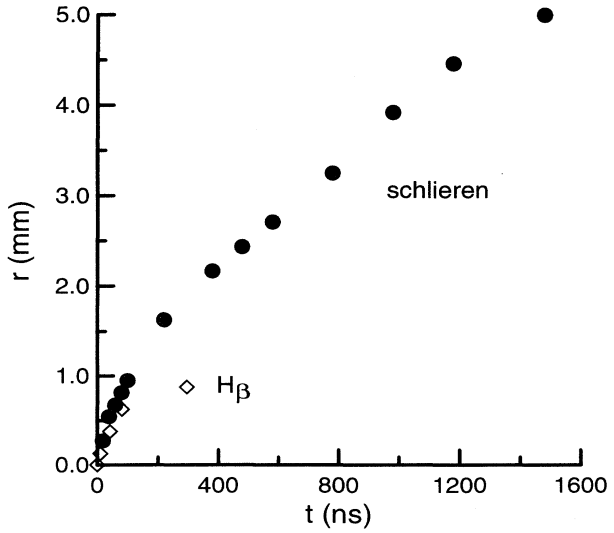

FIG. 10. The positions of the shock front (•) and of regions of maximum H_β luminosity (◇) during the plasma expansion.

Shadow graphic techniques have been developed to follow the propagation farther out, and to observe the evolution of the warm postshock gas [7]. Some of the unusual features seen from 10 to 100 μs after breakdown will be discussed elsewhere.

E. Electron density and temperature

The Abel inversion and the schlieren image data in Figs. 8 and 9 demonstrate that H_β is emitted from a shell behind the shock front which expands outward from the axis. Time-resolved spectra from H_α to H_β may be analyzed to determine its electron density and the electron temperature in this shell. We defer for the moment an examination of whether the plasma is in local thermodynamic equilibrium (LTE) pending an approximate determination of the plasma parameters experimentally, and the application of basic hydrodynamic theory to the problem. If we assume LTE is established immediately after the breakdown pulse, then we can reduce the spectra to extract two quantities: the electron density N_e and the electron temperature T_e. Later we will see that the results of this analysis are consistent with the LTE hypothesis. The widths of the H_α and H_β lines are particularly sensitive to N_e while being relatively insensitive to T_e. The ratio of the total emission intensity of the lines I_ℓ to the bremsstrahlung and radiative recombination continuum I_c over a 100-Å band underlying them depends only on T_e. The details of the methods used are described by Griem [12]. He provides tabulations of Stark broadening coefficients for the Balmer series which relate the full Stark width at half maximum intensity, $\Delta\lambda$, to the electron density N_e with a nominal constant $C(N_e, T_e)$ through

$$N_e = C(N_e, T_e)\ (\Delta\lambda)^{3/2}\ . \tag{1}$$

The electron temperature is determined from the ratio I_ℓ/I_c which may be calculated or taken from graphs for the appropriate lines. Since the spectra are stored in a computer database, this is a straightforward process in principle. In practice, identification of the true continuum level is not possible without detailed spectral modeling for delay times less than 200 ns because the Balmer lines then are so broad that their Stark wings overlap. The continuum in those cases is estimated asymptotically by fitting the profile of H_β or H_α, but the uncertainty in line-to-continuum ratio remains large for the earliest times. T_e can be found from H_α up to 100 000 K, and for H_β up to 50 000 K from this ratio. At the other extreme, when the delays are greater than 2 μs, the continuum is too weak to be a useful diagnostic.

Once an approximate T_e is established, the density N_e is derived from the linewidth. At the earliest times, H_β is too wide, but H_α can be accurately measured. After about 50 ns, H_β measurements provide more accuracy than H_α. Where they overlap, the two techniques yield similar values for N_e. After 3 μs, the width of H_β is about 30 Å, that is, approximately 10× the instrumental width. Exact deconvolution of the instrument response is not necessary for times less than this, but approximate corrections are made in all cases.

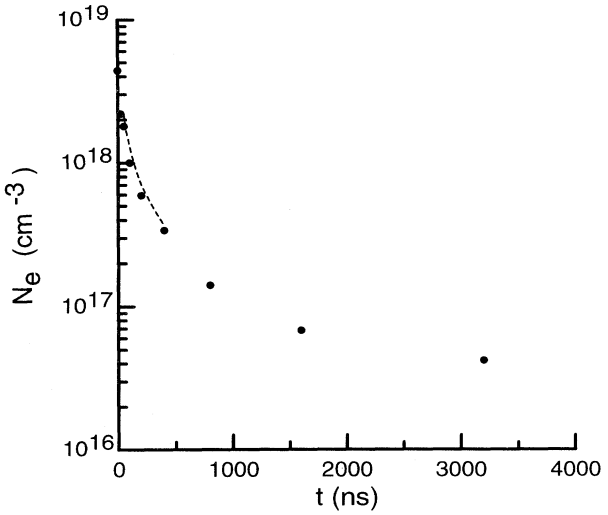

FIG. 11. Electron density N_e measured from the Stark broadening of H_β (•) in the spectrum of the axis of a laser-produced hydrogen plasma at 700 Torr. The curve (- - -) is a theoretical model based on a blast wave calculation.

Figures 11 and 12 show the time-dependence of N_e and T_e from the Balmer series spectra centered on the axis. These axial line-of-sight spectral measurements are actually of two equivalent volumes on opposite sides of the axis, spatially localized in the expanding luminous shell. The initial value for N_e, $4.4 \pm 0.8 \times 10^{18}$ cm^{-3}, is a lower limit. The time resolution of our electronics is approximately 10 ns, and a clearly defined very rapid drop in density with time follows the initial breakdown. Although speculative, it is likely that N_e greatly exceeds

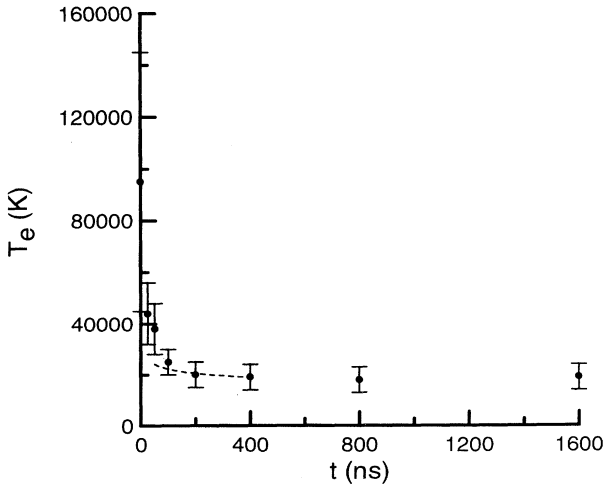

FIG. 12. Electron temperature T_e measured from Balmer series-to-continuum intensity ratios (•) in the spectrum of the axis of a laser-produced hydrogen plasma at 700 Torr. The curve (- - -) is a theoretical model based on a blast wave calculation.

the measured initial value in the first few nanoseconds following the arrival of the Nd:YAG pulse and the establishment of breakdown, and that the measured value is an average dominated by the low-density end of the pulse where the atomic emission is largest. A similar statement can be made about the value of T_e at breakdown, but here the initial temperature may exceed the useful range of the line-to-continuum ratio method. As noted, when the electron density is this high, the Balmer line profiles obscure the true continuum. The line-to-continuum ratio is so small that the temperature is very sensitive to errors in setting the true continuum level. This problem is particularly acute for times up to 50 ns. Over the time interval from 50 ns to 3.2 μs, however, the ratios are all within reasonable range, interference with the continuum measurement from the broadening is not so severe, and the values of T shown in the figures should be almost as reliable as the theory from which they are derived. Griem's estimate of accuracy in T by this method is 10%, and for N_e from linewidths he provides an error estimate of 20%, but suggests that the errors may not actually be so large. In measurements of N_e the errors are dominated by the theory, and not by the actual experimental measurements, which have errors of only a few percent.

III. ANALYSIS

A. Shock phenomena

With the discovery that laser-generated plasmas produced luminous features moving with speeds of several km/s, the most satisfactory theoretical explanations have been based on shock wave phenomena [13]. The Taylor-Sedov blast wave resulting from a laser focused on a solid target, for example, recently was used to investigate blast wave instabilities [14]. A blast wave theory coupled with atomic excitation calculations has been shown to account for the emission spectra of laser-generated plasmas and the temporal development of spectral lines with a variety of gaseous targets, including air, He, and a He-Ar mixture [3]. Based on the success of that approach, and the experimental recognition here that the luminous region of the plasma and the shock front may be distinguished from one another, it is appropriate to compare the results of these experiments with blast wave theories.

A comprehensive summary of basic shock wave theory is given in Ref. [15]. More recent theoretical developments are reviewed by Ostriker and McKee for astrophysical applications [16]. Although the fundamental theory has remained unchanged since its introduction by Taylor [17] and Sedov [18], there are several alternative techniques for computing the blast wave propagation and structure, particularly for nonspherical geometries. A complete model would include the effects of the presence of intense ultraviolet radiation from the initial breakdown, dissociation of a molecular gas, ionization of the atomic gas, radiative loss, and the presence of counterpressure from the background gas. The overall behavior can be accounted for with the simpler approach, suggested by Shah *et al.* [3], of using blast wave theory and Saha ionization-equilibrium theory together. An advantage of this approach is that an analytical series solution exists for the wave with counterpressure in cylindrical geometry [19,20].

The behavior of the laser-produced plasma in H_2 depends on the energy E_0 absorbed from the laser beam by the gas. In a self-similar explosion when the counterpressure is neglected, there is no scale length. In the real case, with an undisturbed gas of background pressure P_0, there is a scale length R_0, set by the ratio E_0/P_0. The expression for the scale length depends on the symmetry. In the case of spherical expansion from a point,

$$R_0 = [E_0/(4\pi P_0)]^{1/3} . \tag{2}$$

At R_0 the internal energy of the ambient gas pushed outward by the shock is equal to the energy deposited by the laser. Similarly, for a cylindrical expansion with the laser energy deposited along a line of length ℓ,

$$R_0 = [E_0/(12\pi P_0 \ell)]^{1/2} . \tag{3}$$

With R_0 defined by Eqs. (2) or (3), the self-similar spherical theory summarized by Zel'dovich and Raizer [15] or Taylor [17] is in agreement with the general solutions found by Sakurai [19,20] and Sedov [18].

Sakurai and Sedov give the shock wave radius R as a solution of a power series equation

$$(C/U)^2 (R_0/R)^\nu = J_0 \left[1 + \lambda_1 (C/U)^2 + \cdots\right] , \tag{4}$$

where C is the speed of sound in the preshock gas, $U = dR/dt$ is the shock wave speed, and J_0 and λ_1 are constants. The exponent ν is 3 for a spherical wave, and 2 for a cylindrical wave. The constants have been evaluated by numerical solution of the hydrodynamic equations and are tabulated in their papers. In the first order approximation with $\lambda_1 = \lambda_2 = \cdots = 0$ the equations are integrable. For a spherical wave

$$R = (4\pi)^{-1/5} (5/2)^{2/5} J_0^{-1/5} \gamma^{1/5} (E/\rho_0)^{1/5} t^{2/5} \tag{5}$$

gives the signature $t^{2/5}$ behavior of a Sedov-Taylor spherical blast wave. The ratio of specific heats, $\gamma = c_p/c_v$, and the initial mass density in the gas, ρ_0, enter the calculation through the sound speed C. For a cylindrical wave, the result is

$$R = (12\pi)^{-1/4} (2)^{1/2} J_0^{-1/4} \gamma^{1/4} (E/\ell\rho_0)^{1/4} t^{1/2} . \tag{6}$$

We will see that our experiments are consistent with the view that the shock is expanding into H_2, for which $\gamma = 1.4$. With 230 mJ absorbed by 700 Torr of H_2 over a length of 5 mm, the shock wave radius for spherical symmetry from Eq. (5) is

$$R = 0.580\, t^{2/5} \tag{7}$$

while in cylindrical symmetry it is

$$R = 0.371\, t^{1/2} \tag{8}$$

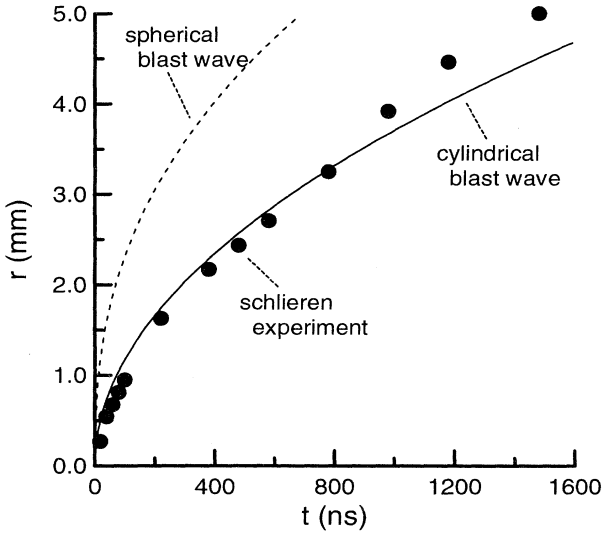

FIG. 13. Comparison of the Sedov-Taylor spherical blast wave, Sakurai cylindrical blast wave, and the observed shock front position.

for times in μs and radii in mm. Both expressions are evaluated and compared with the schlieren measurements in Fig. 13.

The model of blast wave expansion in spherical geometry overestimates the distance of the shock front at all times, and does not have the observed lower velocities (low slope in Fig. 13) at later times. The cylindrical model matches the observations very well. The main source of uncertainty in the experimental data on which this calculation is based is the length of the plasma, but that enters the model as $\ell^{-1/4}$, and the effect of relative errors of $\Delta\ell/\ell$ on the computed radius is reduced by 1/4 of what they would be if the dependence were linear. Consequently, the agreement is confirmation that the blast wave theory in cylindrical geometry accounts for the front observed by schlieren. It also supports the assumption that the expansion is into H_2 rather than H, because the asymptotic velocity that is observed here is close to the speed of sound in the molecular gas. This is not a trivial point, since it would be possible that the radiation emitted by the initial breakdown plasma could dissociate H_2 in advance of the blast wave shock. However, we have seen that only 2% of the incident laser energy is reemitted by the plasma, so that such effects may be important only in the first few ns when the shocked gas volume is small and the energy required for its dissociation is a fraction of the incident pulse energy. The deviation from the cylindrical theory for later times, where the schlieren measurements rise above the theoretical curve, may result from the changing geometry. The plasma source of the shock wave is only 5 mm long, and the deviations appear for times where the radius is comparable to the length of the source.

The Sakurai theory also provides information about the macroscopic conditions behind the shock front. If $x = r/R$ is a dimensionless variable representing distance from the origin r scaled by the shock front position R, then in terms of it the flow velocity u, pressure P, and mass density ρ are given to second order in (C/U) by

$$u = U\,[f_0(x) + (C/U)^2 f_1(x)], \tag{9}$$

$$P = P_0\,(U/C)^2[g_0(x) + (C/U)^2 g_1(x)], \tag{10}$$

$$\rho = \rho_0\,[h_0(x) + (C/U)^2 h_1(x)]\,. \tag{11}$$

The scale of flow is set by the shock speed U; pressure and mass density behind the front are respectively proportional to the pressure P_0 and the mass density ρ_0 before the shock started. The functions f_0, g_0, and h_0 and their second order corrections f_1, g_1, and h_1 may be computed by numerical solution of the hydrodynamic equations or interpolated from tables given by Sakurai [19,20].

In the second order approximation for $t = 100$ ns, the gas is highly compressed at the shock front, $r = R = 1.17$ mm, but at smaller r the density decreases by several orders of magnitude. The rarified gas in the central region is at nearly constant pressure. The temperature calculated from the blast wave model pressure and density is shown in Fig. 14. The temperature in the gas exceeds 10^6 K at the center, increasing from 10^3 K at the front. As the front progresses outward, its speed decreases, the compression behind the front decreases, and the temperature in the gas there decreases. The gas left behind therefore has a strong temperature gradient. According to Zel'dovich and Raizer, the temperature and pressure far from the point of breakdown will be the same as before breakdown, but close to the origin the behavior will follow a power law [15]

$$\rho \sim r^{3/(\gamma-1)}\,, \tag{12}$$

$$T \sim r^{-3/(\gamma-1)}\,. \tag{13}$$

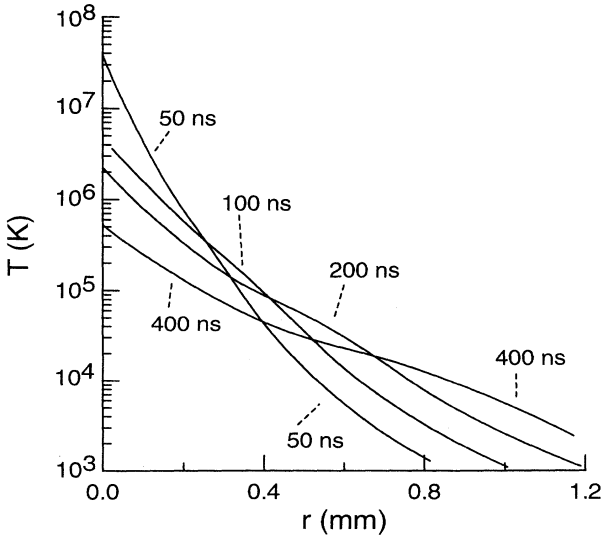

FIG. 14. Gas temperatures behind the shock front, 50, 100, 200, and 400 ns after breakdown, calculated by Sakurai theory in the second order approximation for a cylindrical blast wave.

For an atomic gas with $\gamma = 5/3$ the dependence for T is $r^{-9/2}$. The power law character and the outward progression with time are apparent in a sequence of $T(r)$ curves shown in Fig. 14.

B. Ionization-excitation equilibrium

Figure 15 shows in detail the motion of the H_β shell seen spectroscopically, the high-density region detected in schlieren experiments, and the predicted front calculated with cylindrical blast wave theory. Closer to the center than the compressed gas behind the front, the luminous shell must originate in the lower-density gas where the temperature is sufficient to excite, and ionize, atomic H. The origin and position of the shell is explained by application of the Saha ionization-excitation equilibrium theory to the blast wave model.

Let $\alpha = N_e/N$ be the fraction of the gas that is ionized, where N_e is the density of electrons or protons, and N is the density of atoms before ionization. In collisional equilibrium [21]

$$\alpha^2/(1-\alpha) = N^{-1}\ [2/Z(T)]\left(2\pi mkT/h^2\right)^{3/2} \times \exp(-E'_{\rm H}/kT)\ . \quad (14)$$

Here $E'_{\rm H}$ is the ionization energy of H corrected for plasma interactions, and Z is the partition function for the atom [22]. The neutral atom density N_0 and the electron density N_e are given by

$$N_0 = N\ (1-\alpha)\ , \quad (15)$$

$$N_e = N\ \alpha\ , \quad (16)$$

where α is the solution of Eq. (14). When the electron density is known, the density of the nth excited state of the atom can be calculated from the Boltzmann equation applied to atomic hydrogen,

$$N_0(n) = N_0\ \frac{2n^2}{Z}\ \exp\left(\frac{-E_{\rm H}(1-1/n^2)}{kT}\right)\ . \quad (17)$$

With the blast wave model and Eqs. (14) – (17), the evaluation of N_e, N_0, and the population of the $n = 4$ upper level of the H_β line is a cyclic iteration because of the need to estimate N_e and Z first.

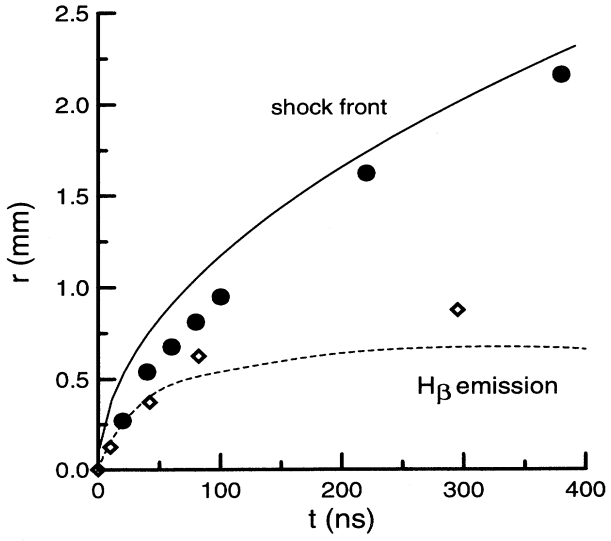

FIG. 15. Location of the luminous atomic hydrogen behind the shock front (◇), compared to the observed shock front (•), Saha equation ionization-equilibrium (- - -) model for H_β emission, and blast wave theory (—).

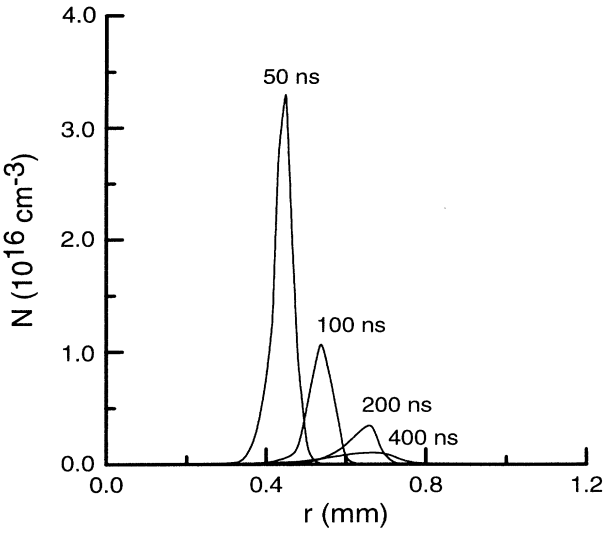

FIG. 16. The luminous atomic hydrogen emits H_β behind the shock front only within a thin shell. The densities of the $n = 4$ state of H for delays of 50, 100, 200, and 400 ns after breakdown are shown.

The radial distributions of the $n = 4$ upper state of H_β calculated for delays of 50 to 400 ns after breakdown are shown in Fig. 16. In agreement with the spatially resolved spectra and Abel-inverted luminosity profiles, H_β is emitted by a shell that moves outward from the axis. It is defined toward larger r by a declining excitation temperature, and toward smaller r by increasing ionization and decreasing neutral atom number density. Figure 17 shows the 100-ns case in detail and demonstrates that the Balmer lines originate from a zone where the electron density is highest. At 100 ns the calculated shell is only 0.1 mm thick, centered around $r = 0.5$ mm.

C. Thermodynamic equilibrium

At several steps through this procedure an implicit assumption of LTE has been made, so, to complete the picture, we need to confirm that LTE does occur under these conditions. First, we show that the collisional rates are high enough that states of interest are in thermodynamic equilibrium. Criteria for complete LTE have been discussed by Griem [22], and others [23,24]. The general form for a pure H plasma is

$$N_e > 10^{15}\sqrt{T}\ , \quad (18)$$

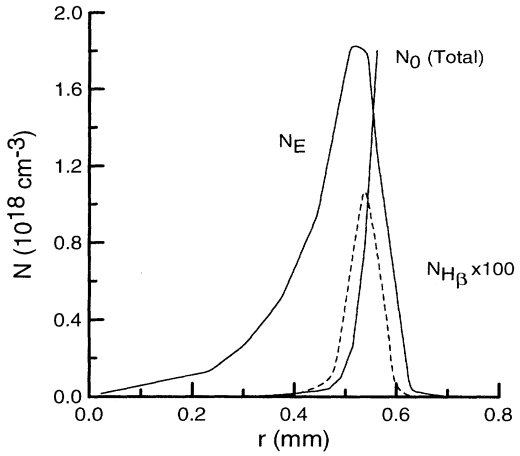

FIG. 17. Neutral H density N_0 behind the shock front 100 ns after breakdown, calculated by Sakurai theory in the second order approximation for a cylindrical blast wave. The electron density N_E and the density of the upper state of the H_β line, (- - -) N_{H_β}, are shown for comparison.

where the electron density N_e is in cm^{-3} and the temperature T is in kelvin. The numerical coefficient here is based on the expressions given by Griem, but it is nearly the same as the coefficients given by others. When this inequality is satisfied, the population of all the excited states will be within 10% of the equilibrium values. Substitution of T for the regions from which H_β is emitted into Eq. (18) confirms that LTE exists. At 50 ns, with $T \approx 25\,000$ K, the critical N_e is 1.6×10^{17} cm^{-3}. The predicted N_e in this region is 20× larger than this critical value. At 400 ns, when $T \approx 19\,000$ K and $N_e = 5\times10^{17}$ cm^{-3}, the critical density is 1.4×10^{17} cm^{-3} and the LTE criterion still is satisfied. Although regions which emit Lyman-α will be slightly farther out in the plasma because the upper state energy is lower, the differences in N_e and T are so small that thermal equilibrium will occur for all the excited states. The criterion for partial LTE applied to this source results in the same conclusion. Nevertheless, Numano [25] has recently used other collisional cross section calculations to reconsider the value of N_e required for complete LTE. The condition which he derives is stronger than the one given by Eq. (18), but the precise threshold depends on the choice of cross section theory and leaves a broad range of uncertainty. Our models fall above the lower bound and confirm LTE for temperatures and densities typical of the emitting regions.

Collisional equilibrium in excited states of H is established quickly in plasmas this dense. For the conditions of the plasma at 50 ns after breakdown, the time constant is $\approx 1.5 \times 10^{-10}$ s based on Griem's expression for the equilibration time for the upper state of the resonance line. This is much faster than the time scale for establishing equilibrium in a typical shock tube because the electron density in the laser-generated plasma is so high and the time constant scales as $N_e^{-1}\exp(E_H/kT)$. Except perhaps in the first fraction of a nanosecond after breakdown, the development of the plasma will follow a succession of states of thermal equilibrium.

Because the plasma has a radial gradient in T, if atoms diffuse in this equilibration time into regions of somewhat different T they will contribute to an anomalous nonthermal population in the new region. Again, from Griem's criteria, the average distance traveled between equilibrating collisions is ≈ 2 μm. For comparison, the thermal gradient in the emitting region is $dT/dr = 3\times10^5$ K/mm or about 600 K across the equilibration distance. Therefore to within a few percent it is meaningful to define a unique temperature at each radial zone in the gas.

D. Shock dissociation of H_2

When the time delay after breakdown is less than a few microseconds, the temperature rises very abruptly behind the shock. For even shorter delays the temperature will be high enough to lead to thermal dissociation of the ambient molecular H_2. Dissociation of H_2 in conventional shock tubes has been studied to determine two- and three-body recombination rates [4,26] over temperature ranges necessary to achieve dissociation. Typically, H_2 is thermally dissociated in a shock pulse for $T > 3500$ K. The effective dissociation rate constant includes both H_2-H and H_2-H_2 two-body collisions, and other many-body effects at higher densities. Recombination depends on three-body collisions and is consequently a much slower process. Once H_2 is dissociated into two H atoms it stays that way, even when the temperature falls later. As an example, 12 ns after breakdown the shock front is moving at 20 mm/μs. It has just passed through a zone 0.4 mm from the axis. Behind the shock the gas temperature is 12 500 K, and it is flowing away from the axis at 17 mm/μs. The shock front is separating from the hot atomic gas it creates. Later, 50 ns after breakdown, the shock front has moved to 0.8 mm, and hot gas from smaller r has expanded outward into the region 0.4 mm from the axis. The temperature there is now higher than it was when the shock front passed through because the hotter gas has moved out into this zone. Thus we see two features, an inner luminous shell, and an outer more refractive dense front. Their progressive movement is the basis for the measurements which were shown in Fig. 10.

At the moment that the front passes, the rate constant K determines the time it will take for the dissociation of H_2 to become significant. For H_2-H_2 collisions the molar concentrations vary according to

$$\frac{d[H_2]}{dt} = -K\,[H_2]^2\,, \tag{19}$$

where K is approximately [27]

$$K = 1.8\times10^{20}\,T^{-3/2}\,\exp[-E_d/(kT)] \tag{20}$$

in units of cm^3 mole^{-1} s^{-1}. The dissociation energy of H_2 is $E_d = 4.48$ eV or 51 954 K. A solution of Eq. (19) yields a decay time to 1/2 the initial density $[H_2]_0$ of

$t_{1/2} = 1/K[H_2]_0$. For this example in the front at 12 ns after breakdown, the time constant $t_{1/2} = 2$ ns. This dissociation time is an upper bound because other dissociation processes can only increase the rate.

We assume here that all of the gas behind the front is promptly dissociated, an assumption that is reasonable early in the history of the postbreakdown gas. The boundary between atomic and molecular gas must be quite sharp, producing a very thin shell of vibrationally excited molecular gas analogous to the H_β shell we have computed for excited atomic states. The difference in the two cases is that, because the H_2 molecule is homonuclear, it does not radiate rapidly from vibrationally excited states of the lower electronic state. The dissociation energy of the molecule is less than the energy needed to populate the first excited electronic states. The region where the molecules are present has no free electrons that could directly populate the excited states by collision without dissociating the molecule first. Consequently, H_2 should not radiate from these laser-generated plasmas.

As the expanding shock front decelerates, the compression and heating behind it fall below a threshold for dissociation of H_2. This occurs when $U \approx 10.7$ mm/μs, about 30 ns after breakdown. The atomic gas produced at that time has an outward flow of 8.9 mm/μs, which becomes the moving boundary between atomic and molecular postplasma gas. The boundary motion decelerates at a nonuniform rate, initially ≈ -200 mm/μs^2. After 1 μs the atomic H extends more than 1 mm from the axis, but its outward flow has nearly stopped. Atomic H from the interior eventually catches up to produce a shell-like feature such as the one apparent at 6 μs and 1.5 mm in the Abel-inverted measurement of Fig. 9.

IV. SUMMARY

In summary, a cylindrical shock wave develops around the breakdown region of a laser-produced plasma in H_2. The atomic gas which appears behind the front is in LTE, and its state is described by the Saha equation and Boltzmann distribution coupled with cylindrical blast wave theory. Immediately after breakdown the region of H_β emission rapidly moves outward. At first the velocities are nearly as high as the shock wave, but after a few hundred nanoseconds the luminous shell almost stops moving while the shock wave itself continues outward and decelerates slowly. After 1 μs the shock velocity drops below the speed of sound, and stops compressing and heating the gas, at which time it includes a spheroid with a diameter of approximately 1 cm.

Atomic H is confined to a 3 mm diameter cylinder within the shock heated spheroid. Typically, 1 mm from the axis and 400 ns after breakdown, the atomic H has density of 2.5×10^{18} cm^{-3} at 5000 K, remarkably similar to the density and temperature of the solar atmosphere at unit optical depth. The atomic densities in these sources are at least two orders of magnitude greater than those produced by a Wood's tube, and offer the possibility of experimentally studying radiative collisions of excited atomic H by spectroscopic means.

ACKNOWLEDGMENTS

The assistance of Aaron Sparks in the laboratory is gratefully acknowledged. This work is supported by the Division of Chemical Sciences, Office of Basic Energy Sciences, Office of Energy Research, U.S. Department of Energy.

[1] T. P. Hughes, *Plasmas and Laser Light* (Adam Hilger, Bristol, 1975), p. 145.
[2] G. M. Weyl, *Laser-Induced Plasmas and Applications*, edited by L. J. Radziemski and D. A. Cremers (Dekker, New York, 1989), p. 1.
[3] P. Shah, A. Biswas, R. L. Armstrong, and L. J. Radziemski, J. Appl. Phys. **68**, 3809 (1990).
[4] R. W. Patch, J. Chem. Phys. **36**, 1919 (1962).
[5] J. L. Lemaire, J. L. Chotin, and F. Rostas, J. Phys. B **18**, 95 (1985).
[6] W. Weise, H. F. Berg, and H. R. Griem, Phys. Rev. **120**, 1079 (1960).
[7] F. Huang, M.S. thesis, University of Louisville, Louisville, 1994.
[8] J. Horrar, M.Eng. thesis, University of Louisville, Louisville, 1993.
[9] J. Kielkopf, in *Spectral Line Shapes*, edited by R. Stamm and B. Talin (Nova Science, New York, 1993), Vol. 7, p. 271.
[10] H. R. Griem, *Plasma Spectroscopy* (McGraw-Hill, New York, 1964), pp. 176–178.
[11] I. H. Hutchinson, *Principles of Plasma Diagnostics* (Cambridge University Press, Cambridge, England, 1987), pp. 124–125.
[12] H. R. Griem, *Plasma Spectroscopy* (McGraw-Hill, New York, 1964), pp. 279–283 and 303–307.
[13] N. Ahmad, B. C. Gale, and M. H. Key, Proc. R. Soc. London Ser. A **310**, 231 (1969).
[14] J. Grun, J. Stamper, C. Manka, J. Resnick, R. Burris, J. Crawford, and B. H. Ripin, Phys. Rev. Lett. **66**, 2738 (1991).
[15] Ya. B. Zel'dovich and Yu. P. Raizer, in *Physics of Shock Waves and High-Temperature Hydrodynamic Phenomena*, edited by W. D. Hayes and R. F. Probstein (Academic, New York, 1966), Vol. I, pp. 93–101.
[16] J. P. Ostriker and C. F. McKee, Rev. Mod. Phys. **60**, 1 (1988).
[17] G. Taylor, Proc. R. Soc. London Ser. A **201**, 175 (1950).
[18] L. I. Sedov, in *Similarity and Dimensional Methods in Mechanics*, edited by Maurice Holt and translated by Morris Friedman from the 4th Russian edition (Academic, New York, 1959).
[19] A. Sakurai, J. Phys. Soc. Jpn. **8**, 662 (1953).
[20] A. Sakurai, J. Phys. Soc. Jpn. **9**, 256 (1954).

[21] K. R. Lang, *Astrophysical Formulae*, 2nd ed. (Springer-Verlag, Berlin, 1980), p. 245.
[22] H. R. Griem, *Plasma Spectroscopy* (McGraw-Hill, New York, 1964), pp 124–142.
[23] A. P. Thorne, *Spectrophysics* (Chapman and Hall, London, 1988), pp. 352–358.
[24] I. H. Hutchinson, *Principles of Plasma Diagnostics* (Cambridge University Press, Cambridge, England, 1987), pp. 197–199.
[25] M. Numano, J. Quant. Spectrosc. Radiat. Transfer **43**, 311 (1990).
[26] I. R. Hurle, A. Jones, and J. L. J. Rosenfeld, Proc. R. Soc. London Ser. A **310**, 253 (1969).
[27] W. C. Gardiner, Jr., and G. B. Kistiakowsky, J. Chem. Phys. **35**, 1765 (1961).

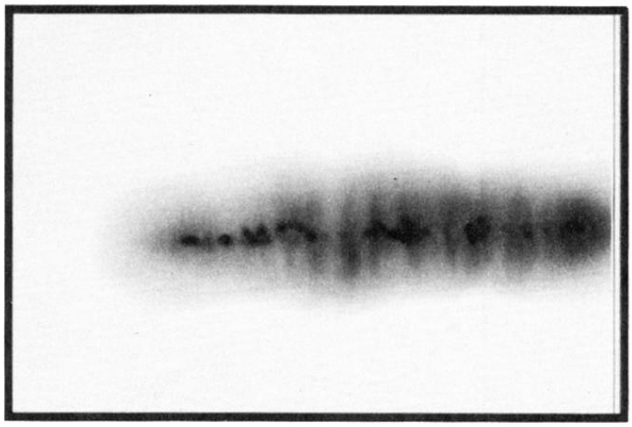

FIG. 3. A plasma in 2.2×10^{19} cm^{-3} H_2 produced by a 300-mJ 1064-nm Nd:YAG focused laser pulse entering from the right. The border defines a region 6×4 mm^2.